HHS Public Access

Author manuscript

*Nat Struct Mol Biol*. Author manuscript; available in PMC 2016 November 16.

Published in final edited form as:

*Nat Struct Mol Biol*. 2016 June ; 23(6): 590–599. doi:10.1038/nsmb.3230.

# Mechanism of extracellular ion exchange and binding-site occlusion in the sodium-calcium exchanger

**Jun Liao**[#1], **Fabrizio Marinelli**[#2], **ChangKeun Lee**[3,4], **Yihe Huang**[3], **José D. Faraldo-Gómez**[2], and **Youxing Jiang**[3,4]

[1]School of Life Science and Technology, ShanghaiTech University, Shanghai, P.R. China.

[2]Theoretical Molecular Biophysics Section, National Heart, Lung and Blood Institute, National Institutes of Health, Bethesda, MD, USA.

[3]Department of Physiology, University of Texas Southwestern Medical Center, Dallas, TX, USA.

[4]Howard Hughes Medical Institute, University of Texas Southwestern Medical Center, Dallas, TX, USA.

[#] These authors contributed equally to this work.

## Abstract

$Na^+/Ca^{2+}$ exchangers utilize the $Na^+$ electrochemical gradient across the plasma membrane to extrude intracellular $Ca^{2+}$, and play a central role in $Ca^{2+}$ homeostasis. Here, we elucidate their mechanisms of extracellular ion recognition and exchange through a structural analysis of the exchanger from *Methanococcus jannaschii* (NCX_Mj) bound to $Na^+$, $Ca^{2+}$ or $Sr^{2+}$ in various occupancies and in an apo state. This analysis defines the binding mode and relative affinity of these ions, establishes the structural basis for the anticipated $3Na^+$:$1Ca^{2+}$ exchange stoichiometry, and reveals the conformational changes at the onset of the alternating-access transport mechanism. An independent analysis of the dynamics and conformational free-energy landscape of NCX_Mj in different ion-occupancy states, based on enhanced-sampling molecular-dynamics simulations, demonstrates that the crystal structures reflect mechanistically relevant, interconverting conformations. These calculations also reveal the mechanism by which the outward-to-inward transition is controlled by the ion-occupancy state, thereby explaining the emergence of strictly-coupled $Na^+/Ca^{2+}$ antiport.



Correspondence should be addressed to: J.L. (liaojun@shanghaitech.edu.cn) or J.D.F.-G. (jose.faraldo@nih.gov) or Y.J (youxing.jiang@utsouthwestern.edu).

Author Contributions

J.L. and Y.J. designed the experimental studies and analyzed the resulting data. J.L., C.L. and Y.H. performed the experimental research. F.M and J.D.F.G. designed the computational research and analyzed the corresponding data. F.M. performed the computational work. J.L., Y.J. F.M. and J.D.F.G. wrote the paper. The authors declare no competing financial interests.

Accession codes

Atomic coordinates and structural factors have been deposited in the Protein Data Bank, with accession numbers 5HWX, 5HWY, 5HXC, 5HXE, 5HYA, 5HXH, 5HXS and 5HXR, as specified in **Tables 2-4**.

## Introduction

$Na^+/Ca^{2+}$ exchangers (NCX) play physiologically essential roles in $Ca^{2+}$ signaling and homeostasis[1-4]. NCX catalyzes the uphill extrusion of intracellular $Ca^{2+}$ across the cell membrane, by coupling this process to the downhill permeation of $Na^+$ into the cell[5,6], with a 3 $Na^+$ to 1 $Ca^{2+}$ stoichiometry[6-11]. This reaction is, however, inherently reversible, its direction being dictated only by the transmembrane electrochemical ion gradients [1]. The mechanism of NCX proteins is therefore highly likely to be consistent with the alternating-access model of secondary-active transport[12]. The basic functional unit for ion transport in NCX consists of ten membrane-spanning segments[13,14], comprising two homologous halves. Each of these halves contains a highly conserved region, referred to as α-repeat, known to be important for ion binding and translocation[15,16]; in eukaryotic NCX, the two halves are connected by a large intracellular regulatory domain[2,15,17,18], which is absent in microbial NCX[15,19] (**Supplementary Fig. 1**).

Despite a long history of physiological and functional studies, the molecular mechanism of NCX has been elusive, owing to the lack of structural information. Our recent atomic-resolution structure of NCX_Mj from *Methanococcus jannaschii* provided the first view of the basic functional unit of an NCX protein[20]. This structure shows the exchanger in an outward-facing conformation and reveals four putative ion-binding sites, denominated internal ($S_{int}$), external ($S_{ext}$), $Ca^{2+}$-binding ($S_{Ca}$) and middle ($S_{mid}$), clustered in the center of the protein and occluded from the solvent[20] (**Fig. 1a-b**). With similar ion exchange properties to those of its eukaryotic counterparts[20,21], NCX_Mj provides a compelling model system to investigate the structural basis for the specificity, stoichiometry and mechanism of the ion-exchange reaction catalyzed by NCX. In this study, we set out to determine the structures of outward-facing wild-type NCX_Mj in complex with $Na^+$, $Ca^{2+}$ and $Sr^{2+}$, at various concentrations. These structures reveal the mode of recognition of these ions, their relative affinities, and the mechanism of extracellular ion exchange, for a well-defined, functional conformation in a membrane-like environment. An independent analysis based on molecular-dynamics simulations demonstrates that the structures capture mechanistically relevant states. These calculations also reveal how the ion occupancy state of the outward-facing exchanger determines the feasibility of the transition to the inward-facing conformation, thereby addressing a key outstanding question in secondary-active transport, namely how the transported substrates control the alternating-access mechanism.

## Results

### Extracellular $Na^+$ binding

The assignment of the four central binding sites identified in the previously reported NCX_Mj structure[20] was hampered by the presence of both $Na^+$ and $Ca^{2+}$ in the protein crystals. To conclusively clarify this assignment, we first set out to examine the $Na^+$ occupancy of these sites without $Ca^{2+}$. Crystals were grown in 150 mM NaCl using the lipidic cubic phase (LCP) technique[20]. The crystallization solutions around the LCP droplets were then slowly replaced by solutions containing different concentrations of NaCl and EGTA (**Methods**). X-ray diffraction of these soaked crystals revealed a $Na^+$-dependent variation in the electron-density distribution at sites $S_{ext}$, $S_{Ca}$ and $S_{int}$, indicating a $Na^+$

occupancy change (**Fig. 1c**). Occupancy refinement indicated two $Na^+$ ions bind to $S_{int}$ and $S_{Ca}$ at low $Na^+$ concentrations (**Fig. 1c**), with a slight preference for $S_{int}$ (**Table 1**). Binding of a third $Na^+$ to $S_{ext}$ occurs at higher concentrations, as no density was observed there at 10 mM $Na^+$ or lower (**Fig. 1c**); $S_{ext}$ is however partially occupied at 20 mM $Na^+$, and fully occupied at 150 mM (**Fig. 1c**). The $Na^+$ occupation at $S_{Ca}$, compounded with the expected $3Na^+$:$1Ca^{2+}$ stoichiometry, implies our previous assignment of the $S_{mid}$ site must be re-evaluated. Indeed, two observations indicate that a water molecule rather than a $Na^+$ ion occupies $S_{mid}$, as was predicted in a recent simulation study[22]. First, the electron density at $S_{mid}$ does not depend significantly on the $Na^+$ concentration. Second, the protein coordination geometry at $S_{mid}$ is clearly suboptimal for $Na^+$ (**Supplementary Fig. 1d**). The water molecule at $S_{mid}$ forms hydrogen-bonds with the highly conserved Glu54 and Glu213 (**Supplementary Fig. 1d**), stabilizing their orientation to properly coordinate multiple $Na^+$ ions at $S_{ext}$, $S_{Ca}$ and $S_{int.}$ It can be inferred from this assignment that Glu54 and Glu213 are ionized, while Asp240, which flanks $S_{mid}$ (and is replaced by Asn in eukaryotic NCX) would be protonated, as indicated by the abovementioned simulation study[22].

## $Na^+$-dependent conformational change

The NCX_Mj structures in various $Na^+$ concentrations also reveal that $Na^+$ binding to $S_{ext}$ is coupled to a subtle but important conformational change (**Fig. 2**). When $Na^+$ binds to $S_{ext}$ at high concentrations, the N-terminal half of TM7 is bent into two short helices, TM7a and TM7b (**Fig. 2a**). TM7b occludes the four central binding sites from the external solution, with the backbone carbonyl of Ala206 coordinating the $Na^+$ ion (**Fig. 2b-d**). However, when $S_{ext}$ becomes empty at low $Na^+$ concentrations, TM7a and TM7b become a continuous straight helix (**Fig. 2a**), and the carbonyl group of Ala206 retracts away (**Fig. 2b-d**). TM7a also forms hydrophobic contacts with the C-terminal half of TM6. These contacts are absent in the structure with $Na^+$ at $S_{ext}$, in which there is an open gap between the two helices (**Fig. 2b**). This difference is noteworthy because TM6 and TM1 are believed to undergo a sliding motion, relative to the rest of the protein, when the transporter switches to the inward-facing conformation[20]. The straightening of TM7ab also opens up a passageway from the external solution to $S_{ext}$ and $S_{mid}$, while $S_{Ca}$ and $S_{int}$ remain occluded (**Fig. 2d**). Thus, the structures at high and low $Na^+$ concentrations represent the outward-facing occluded and partially open states, respectively. This conformational change is dependent on the $Na^+$ occupancy of $S_{ext}$ and occurs when $Na^+$ already occupies $S_{int}$ and $S_{Ca}$. Our crystallographic titration experiment indicates that the $K_{1/2}$ of this $Na^+$-driven conformational transition is ~20 mM. At this concentration, $S_{ext}$ is partially occupied and the NCX_Mj crystal is a mixture of both the occluded and partially open conformations. This structurally-derived $Na^+$ affinity agrees well with the external $Na^+$ concentration required for NCX activation in eukaryotes[1]. The finding that the $Na^+$ occupancy change from 2 to 3 ions coincides with a conformational change of the transporter also provides a rationale to the Hill coefficient of the $Na^+$-dependent activation process in eukaryotic NCX[1,7,8,11].

## Extracellular $Ca^{2+}$ and $Sr^{2+}$ binding and their competition with $Na^+$

To determine how $Ca^{2+}$ binds to NCX_Mj and competes with $Na^+$, we first titrated the crystals with $Sr^{2+}$ (**Methods**). $Sr^{2+}$ is transported by NCX similarly to $Ca^{2+}$ [23,24], and is

distinguishable from $Na^+$ by its greater electron-density intensity. Protein crystals soaked with 10 mM $Sr^{2+}$ and 2.5 mM $Na^+$ revealed a strong electron-density peak at site $S_{Ca}$, indicating binding of a single $Sr^{2+}$ ion (**Fig. 3a**). The $Sr^{2+}$-loaded NCX_Mj structure adopts the partially open conformation observed at low $Na^+$ concentrations. Binding of $Sr^{2+}$, however, excludes $Na^+$ entirely. Crystal titrations with decreasing $Sr^{2+}$ or increasing $Na^+$ demonstrated that $Sr^{2+}$ binds to the outward-facing NCX_Mj with low affinity, and that it can be out-competed by $Na^+$ even at low concentrations (**Supplementary Note 1** and **Supplementary Fig. 2a-b**). Thus, in 100 mM $Na^+$ and 10 mM $Sr^{2+}$, $Na^+$ completely replaced $Sr^{2+}$ (**Fig. 3a**) and reverted NCX_Mj to the $Na^+$-loaded, fully occluded state.

Similar titration experiments showed that $Ca^{2+}$ and $Sr^{2+}$ binding to NCX_Mj are not exactly alike The electron density distribution from crystals soaked in high $Ca^{2+}$ and low $Na^+$, indicates that $Ca^{2+}$ can bind to $S_{mid}$ as well as $S_{Ca}$, with a preference for $S_{Ca}$ (**Fig. 3b**). Binding of $Ca^{2+}$ to both sites simultaneously is highly improbable due to their close proximity, and at least one water molecule can be discerned coordinating the ion (**Fig. 3b**). The partial $Ca^{2+}$ occupancy at $S_{mid}$ is likely caused by Asp240, which flanks this site and can in principle coordinate $Ca^{2+}$. Previous functional and computational studies, however, indicate Asp240 becomes protonated during transport[22]. Indeed, in most NCX proteins Asp240 is substituted by Asn, which would likely weaken or abrogate $Ca^{2+}$ binding to $S_{mid}$. $S_{Ca}$ is therefore the functional $Ca^{2+}$ site. Similarly to $Sr^{2+}$, $Ca^{2+}$ binds with low affinity to outward-facing NCX_Mj and can be readily displaced by $Na^+$ (**Supplementary Note 1** and **Supplementary Fig. 2c**). This finding is consistent with physiological and biochemical data for both eukaryotic NCX and NCX_Mj indicating that the apparent $Ca^{2+}$ affinity is much lower on the extracellular than the cytoplasmic side[21,23,25-27]. Specifically, our crystallographic titration assay indicates $Ca^{2+}$ binds with sub-millimolar affinity, in good agreement with the external apparent $Ca^{2+}$ affinities deduced functionally for cardiac NCX ($K_m$ ~ 0.32 mM)[26] and NCX_Mj ($K_m$ ~ 0.175 mM).[21]

Taken together, these crystal titration experiments demonstrate that the four binding sites in outward-facing NCX_Mj exhibit different specificity: $S_{int}$ and $S_{ext}$ are $Na^+$ specific whereas $S_{Ca,}$ previously hypothesized to be $Ca^{2+}$ specific[20], can also bind $Na^+$, confirming our earlier simulation study[22], as well as $Sr^{2+}$; $S_{mid}$ can also transiently accommodate $Ca^{2+}$ but during transport $S_{mid}$ is most likely occupied by water. The ion-binding sites in NCX_Mj can therefore accommodate up to three $Na^+$ ions or a single divalent ion, and occupancy by $Na^+$ and $Ca^{2+}$ (or $Sr^{2+}$) are mutually exclusive, as was deduced for eukaryotic exchangers[1].

## A structure of NCX_Mj without $Na^+$ or $Ca^{2+}$ bound

An apo state of outward-facing NCX_Mj is likely to exist transiently in physiological conditions, despite the high amounts of extracellular $Na^+$ (~150 mM) and $Ca^{2+}$ (~2 mM). We were able to determine an apo-state structure of NCX_Mj, by crystallizing the protein at lower pH and in the absence of $Na^+$ (**Methods**). This structure is similar to the partially open structure with two $Na^+$ or either one $Ca^{2+}$ or one $Sr^{2+}$ ion, with two noticeable differences. First, TM7ab along with the extracellular half of the TM6 and TM1 swing further away from the protein core (**Fig. 3c**), resulting in a slightly wider passageway into the binding sites. Second, Glu54 and Glu213 side chains rotate away from the binding sites and appear to

form hydrogen-bonds with residues involved in ion coordination in the fully $Na^+$-loaded structure (**Fig. 3d**). Although the binding sites are thus fully accessible to the external solution (**Fig. 3e**), the lack of electron density therein indicates no ions or ordered solvent molecules. This apo structure might therefore represent the unloaded, open state of outward-facing NCX_Mj. Alternatively, this structure might capture a fully protonated state of the transporter, to which $Na^+$ and $Ca^{2+}$ cannot bind. Such interpretation would be consistent with the computer simulations reported below. Indeed, transport assays of NCX_Mj have shown that even in the presence of $Na^+$ or $Ca^{2+}$, low pH inactivates the transport cycle[22].

## Ion occupancy determines the free-energy landscape of NCX_Mj

That secondary-active transporters are able to harness an electrochemical gradient of one substrate to power the uphill transport of another relies on a seemingly simple principle: they must not transition between outward- and inward-open conformations unless in two precise substrate occupancy states. NCX must be loaded either with 3 $Na^+$ or 1 $Ca^{2+}$, and therefore functions as an antiporter; symporters, by contrast, undergo the alternating-access transition only when all substrates and coupling ions are concurrently bound, or in the apo state. The reason why only specific occupancy states permit this transition in a given system, thereby determining its biological function, remains unclear. To examine this central question, we sought to characterize the conformational free-energy landscape of NCX_Mj and to examine its dependence on the ion-occupancy state, using molecular dynamics (MD) simulations. This computational analysis was based solely on the published structure of NCX_Mj[20], independently of the crystallographic studies described above. As it happens, the results confirm that the structures now available are representing interconverting states of the functional cycle of NCX_Mj, while revealing how the alternating-access mechanism is controlled by the ion-occupancy state.

A series of exploratory MD simulations was initially carried out to examine what features of the NCX_Mj structure might depend on the ion-binding sites occupancy. Specifically, we first simulated the outward-occluded form, in the ion configuration we previously predicted[22], now confirmed by the high-$Na^+$ crystal structure described above (**Fig. 1b**). That is, $Na^+$ ions occupy $S_{ext}$, $S_{Ca}$, and $S_{int}$, while D240 is protonated and a water molecule occupies $S_{mid}$. The $Na^+$ ion at $S_{ext}$ was then relocated from the site to the bulk solution (**Methods**), and this system was then allowed to evolve freely in time. The $Na^+$ ions at $S_{Ca}$ and $S_{int}$ were displaced subsequently, and an analogous simulation was then carried out. These initial simulations revealed noticeable changes in the transporter, consistent with those observed in the new crystal structures. The most notable change upon displacement of $Na^+$ from $S_{ext}$ was the straightening of TM7ab (**Fig. 4a**). When 3 $Na^+$ ions are bound, TM7ab primarily folds as two distinct, non-collinear α-helical fragments, owing to the loss of the backbone carbonyl-amide hydrogen-bonds between F202 and A206, and T203 and F207 (**Fig. 4b**). This distortion occludes $S_{ext}$ from the exterior (**Fig. 4d, 4h-i**) and appears to be induced by the $Na^+$ ion itself, which pulls the carbonyl group of A206 into its coordination sphere (**Fig. 4g**). With $S_{ext}$ empty, however, TM7ab forms a canonical α-helix (**Fig. 4a-b, 4g**), thereby creating an opening between TM3 and TM7, which in turn allows water molecules from the external solution to reach into $S_{ext}$ (**Fig. 4e, 4h-i**), i.e. the transporter is no longer occluded. Displacement of $Na^+$ from $S_{Ca}$ and $S_{int}$ induces further changes (**Fig.**

**4c**). The most noticeable is an increased separation between TM7 and TM2 (**Fig. 4f**), previously brought together by concurrent backbone interactions with the $Na^+$ ion at $S_{Ca}$ (**Fig. 4d-e**). TM1 and TM6 also slide further towards the membrane center, relative to the outward-occluded state (**Fig. 4c**). Together, these changes open a second aqueous channel leading directly into $S_{Ca}$ and $S_{int}$ (**Fig. 4f, Fig. 4h-i**). The transporter thus becomes fully outward-open.

To more rigorously characterize the influence of the ion-occupancy state on the conformational dynamics of the exchanger, we carried out a series of enhanced-sampling MD calculations designed to reversibly simulate the transition between the outward-occluded and fully outward-open states, and thus quantify the free-energy landscape encompassing these states (**Methods**). As above, we initially examined three occupancy states, namely with $Na^+$ in $S_{ext}$, $S_{Ca}$ and $S_{int}$, with $Na^+$ only at $S_{Ca}$ and $S_{int}$, and without $Na^+$.

These calculations demonstrate that the $Na^+$ occupancy state of the transporter has a profound effect on its conformational free-energy landscape. When all $Na^+$ sites are occupied, the global free-energy minimum corresponds to a conformation in which the ions are maximally coordinated by the protein (**Fig. 5a, 5c**); TM7ab is bent and packs closely with TM2 and TM3, and so the binding sites are occluded from the solvent (**Fig. 5b**). At a small energetic cost, however, the transporter can adopt a metastable ‘half-open’ conformation in which TM7ab is completely straight and $S_{ext}$ is open to the exterior (**Fig. 5a, 5b**). The $Na^+$ ion at $S_{ext}$ remains fully coordinated, but an ordered water molecule now mediates its interaction with A206:O, relieving the strain on the F202:O–A206:N hydrogen-bond (**Fig. 5c**). This semi-open conformation is nearly identical to that found to be the most probable when $Na^+$ occupies only $S_{Ca}$ and $S_{int}$ ($2 \times Na^+$, **Fig. 5a**), demonstrating that binding (or release) of $Na^+$ to $S_{ext}$ occurs in this metastable conformation. Interestingly, this doubly occupied state can also access conformations in which the second aqueous channel mentioned above, i.e. leading to $S_{Ca}$ between TM7 and TM2 and over the gating helices TM1 and TM6, also becomes open (**Fig. 5b-c**). Crucially, though, the free-energy landscape for this partially occupied state demonstrates that the occluded conformation is no longer energetically feasible (**Fig. 5a**). Displacement of the two remaining $Na^+$ ions from $S_{Ca}$ and $S_{int}$ further reshapes the free-energy landscape of the transporter (No ions, **Fig. 5a**), which now can only adopt a fully open state featuring the two aqueous channels (**Fig. 5b-c**). The transition to the occluded state in this apo state is again energetically unfeasible.

From a mechanistic standpoint, it is satisfying to observe how the open and semi-open states are each compatible with two different $Na^+$ occupancies, explaining how sequential $Na^+$ binding to energetically accessible conformations (prior to those binding events) progressively reshape the free-energy landscape of the transporter; by contrast, the occluded conformation is forbidden unless the $Na^+$ occupancy is complete. This processivity is logical since three $Na^+$ ions are involved, but also implies that in the $Ca^{2+}$-bound state, which includes a single ion, the transporter ought to be able to access all three major conformations, i.e. the outward-open state, in order to release (or re-bind) $Ca^{2+}$, but also the occluded conformation, and thus the semi-open intermediate, in order to transition to the inward-open state. By contrast, occupancy by $H^+$, which as mentioned are not transported,

might be compatible with a semi-open state as well as with the fully open conformation, but should not be conducive to occlusion.

To assess this hypothesis, we carried out enhanced-sampling simulations for the $Ca^{2+}$ and $H^+$-bound states of outward-facing NCX_Mj analogous to those described above for $Na^+$ (see **Supplementary Note 2** and **Supplementary Fig. 3-4** for details on how the structures of the $Ca^{2+}$-bound state was predicted). The calculated free-energy landscape for $Ca^{2+}$-bound NCX_Mj confirms the hypothesis outlined above (1 × $Ca^{2+}$, **Fig. 6a**): consistent with the fact that NCX_Mj transports a single $Ca^{2+}$, the occluded, dehydrated conformation is one of the major energetic minima, but clearly the exchanger can also adopt the semi-open and open states that would be required for $Ca^{2+}$ release and $Na^+$ entry, via either of the aqueous access channels that lead to $S_{ext}$ and $S_{Ca}$ (**Fig. 6b-c**). By contrast, protonation of Glu54 and Glu213 makes the occluded conformation energetically unfeasible, consistent with the fact that NCX_Mj does not transport protons; in this $H^+$-bound state, though, the exchanger can adopt the semi-open conformation captured in the low pH, apo crystal structure (2 × $H^+$, **Fig. 6a-c**).

Taken together, this systematic computational analysis of outward-facing NCX_Mj clearly demonstrates that the alternating-access and ion-recognition mechanisms in this $Na^+/Ca^{2+}$ exchanger are coupled through the influence that the bound ions have on the free-energy landscape of the protein, which in turn determines whether or not the occluded conformation is energetically feasible. This occluded conformation, which is a necessary intermediate between the outward and inward-open states, and which entails the internal dehydration of the protein, is only attainable upon complete occupancy of the binding sites.

## Discussion

The alternating-access hypothesis implicitly dictates that the switch between outward- and inward-open conformations of a given secondary-active transporter must not occur unless the appropriate type and number of substrates are recognized. This control mechanism is functionally crucial, as it precludes the backflow of the species that is transported uphill, and also prevents the dissipation of the driving electrochemical gradients. It is however also non-trivial: antiporters, for example, do not undergo the alternating-access transition without a cargo, but this is precisely how membrane symporters reset their transport cycles. Similarly puzzling is that a given antiporter will undergo this transition upon recognition of substrates of different charge, size and number. Yet, when multiple species are to be co-translocated, by either an antiporter or a symporter, partial occupancies must not be conducive to the alternating-access switch. Here, we have provided novel insights into this intriguing mechanism of conformational control through structural studies and quantitative molecular simulations of a $Na^+/Ca^{2+}$ exchanger.

Specifically, our studies of NCX_Mj reveal the mechanism of forward ion exchange (**Fig. 7**). The internal symmetry of outward-facing NCX_Mj and the inward-facing crystal structures of several $Ca^{2+}/H^+$ exchangers[20,28-30] indicate that the alternating-access mechanism of NCX proteins entails a sliding motion of TM1 and TM6 relative to the rest of the transporter. Here, we demonstrate that conformational changes in the extracellular region of

the TM2-TM3 and TM7-TM8 bundle precede and are necessary for the transition, and are associated with ion recognition and/or release. The most apparent of these changes involves the N-terminal half of TM7 (TM7ab); together with more subtle displacements in TM2 and TM3, this change in TM7ab correlates with the opening and closing of two distinct aqueous channels leading into the ion-binding sites from the extracellular solution. Interestingly, the bending of TM7 associated with the occlusion of the ion-binding sites also unlocks its interaction with TM6, and thus enables TM6 and TM1 to freely slide to the inward-facing conformation. We anticipate that the intracellular ion-exchange process involves analogous conformational changes.

The crystal structures of NCX_Mj reported here, with either $Na^+$, $Ca^{2+}$, $Sr^{2+}$ or $H^+$ bound, capture the exchanger in different conformational states. These states can only represent a subset among all possible, but they ought to reflect inherent preferences of the transporter, modulated by the experimental conditions. For example, in the crystal of NCX_Mj in LCP, the extracellular half of the gating helices (TM6 and TM1) form a lattice contact, which might ultimately restrict the degree of opening of the ion-binding sites in some cases (e.g. in the apo, low pH structure). Nonetheless, the calculated free-energy landscapes, derived without knowledge of the experimental data, reassuringly confirm that the crystallized structures correspond to mechanistically relevant, interconverting states. The simulations also demonstrate how this landscape is drastically re-shaped upon each ion-binding event. Indeed, we show that it is the presence or absence of the occluded state in this landscape that explains the antiport function of NCX_Mj and its $3Na^+$:$1Ca^{2+}$ stoichiometry. We posit that a similar principle might govern the alternating-access mechanism in other transporters; that is, we anticipate that for both symporters and antiporters, it is the feasibility of the occluded state, encoded in the protein conformational free-energy landscape and its dependence on substrate binding, that ultimately explains their specific coupling mechanisms.

In multiple ways, our findings provide an explanation for, existing functional, biochemical and biophysical data for both NCX_Mj and its eukaryotic homologues. The striking quantitative agreement between the ion-binding affinities inferred from our crystallographic titrations and the $K_m$ and $K_{1/2}$ values previously deduced from functional assays has been discussed above. Consistent with that finding, mutations that have been shown to inactivate or diminish the transport activity of NCX_Mj and cardiac NCX[16,31-34] perfectly map to the first ion-coordination shell in our NCX_Mj structures (**Supplementary Fig. 4c-d**). The crystallographic data also provides the long-sought structural basis for the ‘two-site’ model proposed to describe competitive cation binding in eukaryotic NCX[8,35], underscoring the relevance of these studies of NCX_Mj as a prototypical $Na^+/Ca^{2+}$ exchanger. Specifically, our crystal titrations suggest that, during forward $Na^+/Ca^{2+}$ exchange, sites $S_{int}$ and $S_{Ca}$, which $Ca^{2+}$ and $Na^+$ compete for, can be grouped into one; $Na^+$ binding to these sites does not require high $Na^+$ concentrations, and two $Na^+$ ions along with a water molecule (at $S_{mid}$) are sufficient to displace $Ca^{2+}$, explaining the Hill coefficient of ~2 for $Na^+$-dependent inhibition of $Ca^{2+}$ fluxes[35]. The $S_{ext}$ site, by contrast, might be thought as an activation site for inward $Na^+$ translocation, since this is where the third $Na^+$ ion binds at high $Na^+$ concentration, enabling the transition to the occluded state. Interestingly, binding of $Ca^{2+}$ to $S_{mid}$ appears to be also possible, but available evidence indicates that this event transiently

blocks the exchange cycle[22]. Indeed, structures of NCX_Mj bound to $Cd^{2+}$ or $Mn^{2+}$, both of which inhibit transport, show these ions at $S_{mid}$[20]; by contrast, $Sr^{2+}$ binds only to $S_{Ca}$, and accordingly, is transported by NCX similarly to calcium[23,24].

Lastly, our theory that occlusion of NCX_Mj is selectively induced upon $Ca^{2+}$ or $Na^{+}$ recognition is consonant with a recent analysis of the rate of hydrogen-deuterium exchange (HDX) in NCX_Mj, in the presence or absence of these ions[31], in conditions that favor outward-facing conformations[20,21]. Specifically, saturating amounts of $Ca^{2+}$ or $Na^{+}$ resulted in a noticeable slowdown in the HDX rate for extracellular portions of the α-repeat helices. We interpret these observations as reflecting that the solvent accessibility of the protein interior is diminished upon ion recognition, consistent with our finding that opening and closing of extracellular aqueous pathways to the ion-binding sites depend on ion occupancy state. In addition, the increased compactness of the protein tertiary structure in the occluded state would also slow down the dynamics of the secondary-structure elements, and thus further reduce the HDX rate. Our data would also explain the observation that the reduction in the HDX rate is comparable for $Na^{+}$ and $Ca^{2+}$, as well as the finding that the degree of deuterium incorporation remains non-negligible even under saturating ion concentrations. As the calculated free-energy landscapes show, $Na^{+}$ and $Ca^{2+}$ induce the occlusion of the transporter in a comparable manner, and yet the ion-bound states retain the ability to explore conformations that are partially or fully open to the extracellular solution, precisely so as to be able to unload and re-load the substrates.

## Methods

### Protein expression, purification and crystallization

NCX_Mj was expressed, purified and crystallized as previously described[20]. Briefly, the NCX_Mj gene with a C-terminal hexa-histidine tag was subcloned into the pQE60 vector and expressed in *Escherichia coli* BL21(DE3)plysS. Harvested cells were homogenized and incubated in buffer containing 50 mM HEPES pH 7.2, 50 mM NaCl, 12 mM KCl, 10 mM CaCl2, 40 mM DDM. After incubation at room temperature (RT) for 3.5 hours, the supernatant was collected by centrifugation and loaded onto a Talon $Co^{2+}$ affinity column (Clontech). The non-specifically bound contaminates on the column were washed with buffer containing 50 mM HEPES pH 7.2, 50 mM NaCl, 12 mM KCl, 10 mM CaCl2, 15 mM imidazole, and 1 mM DDM. The bound NCX_Mj was eluted by increasing the imidazole concentration to 300 mM. The eluate was treated with thrombin to remove the hexa-histidine tag and dialyzed against 20 mM HEPES pH 7.2, 50 mM NaCl, 12 mM KCl, 10 mM $CaCl_2$, and 1 mM DDM at RT overnight. After overnight digestion the sample was loaded onto a second $Co^{2+}$ affinity column to remove any free hexa-histidine tag and contaminant proteins. NCX_Mj in the flow-through was collected and further purified by gel filtration using a Superdex-200 (10/300) column (GE Healthcare) in 20 mM HEPES pH 7.2, 50 mM NaCl, 12 mM KCl, 10 mM $CaCl_2$ and 0.5 mM DDM. The purified protein was then concentrated to 40 mg/ml for crystallization.

Native NCX_Mj was crystallized using the lipidic cubic phase (LCP) technique, as previously described[20,36]. Concentrated NCX_Mj was first reconstituted into 1-oleoyl-rac-glycerol (Sigma) in a protein:lipid weight ratio of 1:1.5, using the two-syringe method[36].

Protein-laden LCP droplets of 35 nL were dispensed onto Corning 96-well protein-crystallization plates and overlaid with 5 μL of precipitant solution containing 40-42% PEG 400, 100 mM MES pH 6.5, 100 mM NaAc. Crystals were observed after 48 hours and grew to full size after 2 weeks. The native crystals belong to space group $P2_12_12_1$ with a cell dimension of a=49.5Å, b=72.9Å and c=96.2Å, and contain one subunit per asymmetric unit. As the LCP droplet accounts for less than 1% of the total crystallization volume, the salt composition in the crystallization condition was determined mainly by the overlaying solution, and estimated to have 150 mM $Na^+$ (from MES buffer and NaAc) and 30 μM $Ca^{2+}$ (from LCP droplet). In these concentration conditions (high $Na^+$ and low $Ca^{2+}$) $Ca^{2+}$ does not bind to NCX_Mj (as shown in our crystallographic titration experiments) and thus this native crystal structure represents NCX_Mj in 150 mM $Na^+$. The native crystals were used in all subsequent titration experiments to define low-$Na^+$, $Ca^{2+}$ and $Sr^{2+}$-loaded structures.

To obtain the apo crystal form, the protein was first purified in a solution containing 20 mM Hepes-Tris pH 7.2, 100 mM NMDG, 10 mM $CaCl_2$ and 0.5 mM DDM. The crystals were obtained in LCP with crystallization solution containing 200 mM KAc, pH 4.0, 35% PEG400. The apo NCX_Mj crystals belong to space group C2 with a cell dimension of a=164.2Å, b=46.8Å, c=97.0 Å and β=106.2°, and contain two protein subunits per asymmetric unit.

## Crystal titrations

Once the native crystals reached their full size, the crystallization solutions overlaying lipid/protein droplets were gradually replaced by titration solutions through multiple steps of solution exchange. In general, 2-3 μL of existing crystallization solutions (normally in 5 μL) were replaced by the same volume of titration solutions, followed by overnight equilibration. The same procedures were repeated 6-10 times until the ion components in the crystal drops reached the targeted concentrations. For titration experiments to define concentration-dependent $Na^+$ binding, the titration solutions contained 100 mM MES-Tris pH 6.5, 44% PEG400, 10 mM EGTA and a 100 mM mixture of NaAc and CsAc, in the following proportions: 100 mM CsAc; 90 mM CsAc and 10 mM NaAc; 80 mM CsAc and 20 mM NaAc; and 100 mM NaAc. Note that $Cs^+$ does not bind NCX proteins and is commonly used as a $Na^+$ substituent to maintain the ionic strength of the solutions. As complete removal of $Na^+$ would deteriorate the crystals, we had to maintain a minimum $Na^+$ concentration of about 2.5 mM in the crystal drops. The final $Na^+$ concentrations in this set of titration experiments were about 2.5, 10, 20 and 100 mM, respectively. It is worth noting that the observed $Na^+$-dependent conformational change occurs while the proteins are in crystal form and embedded in lipid.

In the titration experiments carried out to define the mode of divalent cation binding and competition with $Na^+$, the soaking solutions contained 100 mM MES-Tris pH 6.5, 44% PEG400, 100 mM mixture of CsAc and NaAc and various concentrations of $XCl_2$, where X=$Ca^{2+}$ or $Sr^{2+}$, in the following proportions: 100 mM CsAc and 10 mM $XCl_2$; 100 mM CsAc and 1 mM $XCl_2$; 100 mM CsAc and 0.1 mM $XCl_2$; 90 mM CsAc, 10mM NaAc and 10mM $XCl_2$; and 100 mM NaAc and 10 mM $XCl_2$. After multiple steps of solution

exchanges, the final soaking conditions contained 0.1, 1, or 10 mM of $X^{2+}$ together with 2.5 mM $Na^+$; or 10 mM $X^{2+}$ together with 2.5, 10 or 100 mM $Na^+$.

### Data collection and structure determination

After soaking crystals were mounted on 100-μm Mitegen Microloops and frozen in liquid nitrogen. All diffraction data were collected at the Advanced Photon Source (APS) GM/CA-CAT beamlines 23ID-B or 23ID-D using a beam size of 35 μm × 50 μm. Data were processed and scaled using HKL2000[37] and the structures were determined by molecular replacement in PHASER[38] using our previously published NCX_Mj structure (PDB code 3V5U)[20] as a search model. Model building was completed using COOT[39] and structure refinement was performed with PHENIX[40]. The data sets from crystals soaked in solutions containing 2.5 to 100 mM $Na^+$ were collected using an X-ray wavelength of 1.033Å; the crystal grown with 150 mM $Na^+$, and those soaked with $Ca^{2+}$ and $Sr^{2+}$ solutions, were obtained with a wavelength of 0.9793 Å. Lastly, the data from the crystal grown at low pH with no $Na^+$ or $Ca^{2+}$ were collected with a 2.0-Å wavelength beam. The resulting statistics for data collection and refinement are shown in **Tables 2-4**. All structure figures were prepared in PyMOL (The PyMOL Molecular Graphics System, Version 1.5.0.4 Schrödinger, LLC.). The ion passageways in low- and high-$Na^+$ structures as well as the apo state were analyzed using the program CAVER[41]. Due to the variation in diffraction resolution and intensity among crystals, ion-occupancy comparisons were made on the basis of the diffraction data obtained in the titration experiments scaled against a common reference data before map calculation. The NCX_Mj crystal obtained with 2.5 mm $Na^+$ only was used as the reference.

### Conventional molecular dynamics (MD) simulations

Conventional (i.e. not enhanced) MD simulations were carried out with NAMD 2.7-2.9 [42] at constant temperature (298 K), pressure (1 atm), and membrane surface area (~69 $Å^2$ per lipid),and with periodic boundaries in all directions. All calculations used the standard CHARMM27/CMAP force field[43,44], except for NBFIX corrections for the interaction between carboxylate-oxygens and $Na^+$ interaction[22] or $Ca^{2+}$ (**Supplementary Note 3, Supplementary Fig. 5**). Electrostatic interactions were calculated using PME with a real-space cut-off of 12 Å; the same cut-off distance was used for all van der Waals interactions.

Five ion-occupancy states of the transporter were considered, namely with 3 $Na^+$, 2 $Na^+$, 2 $H^+$ or 1 $Ca^{2+}$, and with no ions bound; in all cases Asp240 is protonated[22]. For the 3×$Na^+$ state, we reanalyzed a 200-ns trajectory of NCX_Mj reported previously[22]. NCX_Mj had been embedded in a POPC lipid membrane using GRIFFIN[45]. The initial configuration of the 2×$Na^+$ state was generated from an equilibrated configuration of 3×$Na^+$ state, from which the $Na^+$ ion at $S_{ext}$ was displaced by means of a slow alchemical transformation that annihilates the bound ion and recreates it in the bulk solution (in the same simulation box). The resulting 2×$Na^+$ state was simulated for 250 ns. Similarly, the state with no $Na^+$ bound was generated from an equilibrated configuration of the 2×$Na^+$ state, from which the remaining $Na^+$ ions were displaced; this state was again simulated for 250 ns. For the 2×$H^+$ state, an initial configuration was generated from an equilibrated configuration of the 3×$Na^+$ state, by gradually annihilating the $Na^+$ ions from the binding sites and creating protonated

E54 and E213 side chains; concurrently, acetic acid molecules in the bulk solution (in the same simulation box) were deprotonated and $Na^+$ ions introduced. A second initial configuration of the $2\times H^+$ state was obtained from an equilibrated configuration of the simulation with no ions bound, by slowly transforming deprotonated E54 and E213 into their protonated form, while doing the opposite to acetic acid molecules in the bulk solution. These two initial configurations of the $2\times H^+$ state were then equilibrated for 800 ns. All annihilation/creation simulations were carried out using the FEP module of NAMD; and comprised 32-50 intermediate simulations of 400 ps each, for each transformation. A soft-core van der Waals potential with a radius-shifting coefficient of 2 $Å^2$ was used. The annihilated $Na^+$ ions were confined within their corresponding binding sites using flat-bottom distance restraints. Specifically, the $Na^+$ in $S_{ext}$ was concurrently maintained within 4 Å of E54:Cδ, A206:C, S77:Cβ, T209:Cβ and S210:Cβ. The $Na^+$ ions in $S_{Ca}$ and $S_{int}$ were concurrently kept within 4 Å of the E213:Cδ and A47:C, respectively. The $Na^+$ ions and acetic acid molecules in the bulk solution were kept at a distance greater than 37 Å from the membrane center. Finally, the initial configuration of the $Ca^{2+}$ state was generated on the basis of the published NCX_Mj X-ray structure[20] by placing $Ca^{2+}$ in the $S_{Ca}$ site and two water molecules coordinating $Ca^{2+}$ at and near the $S_{mid}$ site, so as to satisfy the expected coordination geometry (see **Supplementary Note 2, Supplementary Fig. 3-4**). This configuration was initially equilibrated through a series of simulations in which RMSD-based restraints of gradually diminishing strength were applied to the protein Cα atoms as well the side-chains involved in $Ca^{2+}$ coordination. A 250 ns equilibration was then carried without any restraints.

## Enhanced-sampling MD simulations

Free-energy landscapes were calculated using Bias-Exchange Well-Tempered Metadynamics (BE-WT-MetaD)[46,47], using GROMACS4.5.5/PLUMED[48,49]. The force-field and simulation conditions were equivalent to those employed in the unbiased MD simulations. The accumulated simulation time for each of the ion-occupancy states studied was 1.6 μs. Each of these calculations consisted of 16 concurrent, interdependent simulations (or replicas); in 15 of these replicas, a WT-MetaD biasing potential was applied on different subsets of collective variables, as specified below, while the remaining replica was unbiased. Attempts to exchange coordinate configurations among replicas were made every 2-5 ps, using the Metropolis criterion[46]. The inputs for each calculation were equilibrated configurations extracted from the unbiased MD simulations.

The choice of collective variables to be biased in the BE-WT-MetaD simulations was also based on analysis of the unbiased MD trajectories (**Fig. 4g-i**). Specifically, to enhance the reversible opening and closing of the water channels reaching from the extracellular bulk solution into either the $S_{ext}$ or the $S_{Ca}$ binding sites, we employed the following time-dependent collective variable (**Fig. 4h-i**):

$$V_{1,2}(t) = \frac{\beta}{ln \sum_i exp\{\beta / r_i(t)\}} \quad \text{(Eq. 1)}$$

where $r_i$ denotes the distance between the oxygen atom of each water molecule in the system $i$ and the center of the binding site considered ($V_1$ for $S_{ext}$, $V_2$ for $S_{Ca}$), and $\beta$ is 10-100 nm. When the binding site was occupied, the ion was used to define its center. If the site was empty, its center was defined as the center-of-mass of the oxygen atoms coordinating the ion if bound. Bound water molecules at or near $S_{mid}$ (coordinating the $Na^+$ or $Ca^{2+}$ ions) were not considered.

To enhance the reversible formation and disruption of selected backbone hydrogen bonds in TM7ab (**Fig. 4g**), we used an analogous collective variable:

$$V_3(t) = \frac{\beta}{ln \sum_{ij} exp\{\beta / r_{ij}(t)\}} \quad \text{(Eq. 2)}$$

In this case, the index $i$ denotes atoms P202:O and T203:O, while the index $j$ denotes atoms A206:N and P207:N. To preclude the artificial unraveling of TM7ab driven by this bias, an upper-bound $V_3^{max}$ equal to 0.7 nm was imposed with a boundary potential of the form $k(V_3(t) - V_3^{max})^4$ if $V_3(t) > V_3^{max}$, where $k = 10^5$ nm$^{-4}$ kJ/mol. In addition, to control the bending and straightening of TM7ab more globally, we used the following path-collective variables[50]:

$$V_4(t) = \frac{exp\{-\lambda d_1(t)\} + 2\, exp\{-\lambda d_2(t)\}}{exp\{-\lambda d_1(t)\} + exp\{-\lambda d_2(t)\}} \quad \text{(Eq. 3)}$$

$$V_5(t) = -\frac{1}{\lambda} ln\left[exp\{-\lambda d_1(t)\} + exp\{-\lambda d_2(t)\}\right] \quad \text{(Eq. 4)}$$

where $d_1$ and $d_2$ denote the mean-square-differences between the conformation of TM7ab and either the straight or bent conformations, respectively, and $\lambda = 100$ nm$^{-2}$. Note that $V_4$ is by definition confined between a lower ($V_4 \sim 1$) and upper bound ($V_4 \sim 2$)[50]; to confine the exploration of $V_5$, an upper value $V_5^{max}$ of 0.020-0.025 nm$^2$ was imposed with boundary potential of the form $k(V_5(t) - V_5^{max})^4$ if $V_5(t) > V_5^{max}$, where $k = 10^{11}$ nm$^{-8}$ kJ/mol. The mean-square-differences $d_1$ and $d_2$ comprise the backbone atoms of residues 198-211 as well as the side chain carbon atoms of residues P207 and L211.

A boundary potential was also applied to confine the ions and water molecule bound to $S_{ext}$, $S_{Ca}$, $S_{int}$ and $S_{mid}$ to their corresponding binding sites. Specifically, the variable confined was:

$$V_c(t) = \sum_i \frac{1 - [r_i(t)/r_0]^8}{1 - [r_i(t)/r_0]^{10}} \quad \text{(Eq. 5)}$$

where $r_i$ denotes the distance between the ion and each of its coordinating oxygen atoms; $r_0$ was set to 0.24 nm for the $Na^+$ ions, and to 0.30 nm for $Ca^{2+}$. Note that the upper-bound value of $V_c$ is, by definition, approximately the coordination number in the bound state, whereas $V_c$ becomes 0 as the ion becomes unbound. For the $Na^+$ ion bound to $S_{ext}$ and $S_{int}$, therefore, a lower bound value $V_c^{min} = 4.3$ was imposed with potential of the form $k\,(V_c(t) - V_c^{min})^4$ when $V_c(t) < V_c^{min}$, where $k = 2500$ kJ/mol. An analogous restraint was used for the $Na^+$ ion at $S_{Ca}$, with $V_c^{min} = 4.75$. Similarly, for the $Ca^{2+}$ ion at $S_{Ca}$ a lower bound value $V_c^{min} = 7.4$ was imposed with a potential of the form $k\,(V_c(t) - V_c^{min})^2$ when $V_c(t) < V_c^{min}$, with $k = 400$ kJ/mol. Note that these restraints do not perturb the chemical structure of the ion-coordination sphere when the ion is bound, i.e. $V_c(t) > V_c^{min}$. The displacement of the bound water molecules in the ion-coordination sphere by equivalent water molecules in the solvent was prevented similarly.

The specific sets of collective variables biased in each of the replica WT-MetaD simulations, as well as further details on the biasing potentials introduced, are specified in **Supplementary Table 1**.

## Derivation of conformational free-energy landscapes

To translate the data gathered in the BE-WT-MetaD simulations into conformational free-energy landscapes, we sought to identify a low-dimensional representation of the data that is nevertheless also intuitive and representative. We ultimately settled on two structure-based descriptors of the degree of opening of the each of the aqueous channels leading to the ion-binding sites (**Fig. 4**), defined as:

$$S_{1,2} = \frac{\beta}{ln \sum_{ij} exp\ \{\beta / r_{ij}\}} \quad \text{(Eq. 6)}$$

where $r_{ij}$ denotes a set of pairwise distances for specific Cα atoms in the protein, for a given simulation snapshot. For $S_1$, index $i$ refers to the Cα of residues 198 to 209 in TM7, while index $j$ refers to those in residues 66 to 80 and 290 to 297, in TM3 and TM10, respectively. For $S_2$, index $i$ refers to the Cα of residues 51 to 64 in TM2, while index $j$ refers to those in residues 177 to 193 and 198 to 209, in TM6 and TM7, respectively. Therefore, $S_1$ describes the effective separation between TM7 and TM3/TM10, on the extracellular half of the protein, and thus reports on the accessibility to the $S_{ext}$ site. Analogously, $S_2$ measures the separation between TM2 and TM6-TM7, also on the extracellular side, and thus reports on the accessibility to $S_{Ca}$.

The conformational free energy of NCX_Mj as a function of $S_1$ and $S_2$ was then computed for each ion-occupancy state separately (**Figs. 5a, 6a**). These landscapes were obtained through reweighting of the biased probability distribution from the BE-WT-MetaD sampling, using the WHAM method[51]; through this approach we combine the statistics gathered in all replicas, and can consider alternate free-energy projections[49,52,53].

To correct the landscape calculated for the $Ca^{2+}$-bound state (**Fig. 6a**) on account of the excess amount of charge transferred from the ion to the protein (**Supplementary Note 4,**

**Supplementary Fig. 6**), we reprocessed all the sampling obtained during the original BE-WT-MetaD simulations, introducing in the WHAM equations a re-weighting factor $w$ for each configuration $\boldsymbol{X}$:

$$w(\boldsymbol{X}) \propto exp\left\{-\frac{U_{\mathrm{c}}(\boldsymbol{X}) - U(\boldsymbol{X})}{k_{\mathrm{B}}T}\right\} \quad \text{(Eq. 7)}$$

where $U$ denotes the 'uncorrected' CHARMM27/NBFIX potential-energy function, and $U_{\mathrm{c}}$ denotes the corrected function. To calculate $U_{\mathrm{c}}$ (**X**), the charge of $Ca^{2+}$ was reduced to +1.8$e$ from its standard value of +2$e$, and the difference was distributed among the surrounding protein residues (as specified in **Supplementary Note 4**). To minimally alter the charge-distribution used in the original CHARMM27 force-field, the charge added to each protein atom was proportional to the absolute value of its uncorrected charge.

The statistical errors for all free-energy landscapes are provided in **Supplementary Fig. 7**.

### Derivation of representative structures and water-density maps

Representative structures and water-density iso-surfaces (**Fig. 5b-c, Fig. 6b-c)** were derived for each BE-WT-MetaD simulation by clustering all sampling[54] in the multi-dimensional space of $V_1$, $V_2$, and $V_4$ (**Eq. 1-3**), plus a descriptor $S_3$ of the proximity between TM6-TM7 and TM2-TM3/TM10, on the extracellular side of the protein. More precisely:

$$S_3 = \sum_{ij} \frac{1 - [r_{ij}(t)/r_0]^8}{1 - [r_{ij}(t)/r_0]^{12}} \quad \text{(Eq. 8)}$$

where $r_0$ = 7.5 Å, and $r_{ij}$ denotes a specific set of pairwise Cα distances, for a given simulation snapshot. Similarly to $S_1$ and $S_2$ (**Eq. 6**), index $i$ refers to Cα atoms in the extracellular halves of TM6 and TM7, while index $j$ refers to Cα atoms in the extracellular halves of TM2, TM3, and TM10. We thus obtained[54] ~2,000 clusters for each of the simulation systems (using RMSD cut-off values of 1.3 Å for $V_1$ and $V_2$, 0.1 Å for $V_4$, and 6.25 Å for $S_3$). Using the WHAM equations, we calculated the relative free energy of each of these clusters, and then identified the major basins in this space with the MCL method[55,56] (with $p$ = 1.4.) Water occupancy maps were calculated for each of these major free-energy basins, only using the sampling gathered by the unbiased replicas.

## Supplementary Material

Refer to Web version on PubMed Central for supplementary material.

## Acknowledgements

The experimental results reported in this article derive from measurements made at the Advanced Photon Source of the Argonne National Laboratory, GM/CA (23ID), which is operated by UChicago Argonne, LLC, for the U.S. Department of Energy, Office of Biological and Environmental Research, under contract DE-AC02-06CH11357. We thank the beamline staff for their assistance in data collection. This work was supported in part by the Howard Hughes Medical Institute; by grants from the National Institutes of Health (R01GM079179 to Y. J.) and the Welch

Foundation (Grant I-1578 to Y. J.); by the General Program of the National Natural Science Foundation of China (Project 31470817 to J. L.); and by the Division of Intramural Research of the National Heart, Lung and Blood Institute, National Institutes of Health (to F.M. and J.D.F.-G.).

## References

1. Blaustein MP, Lederer WJ. Sodium/calcium exchange: its physiological implications. Physiol Rev. 1999; 79:763–854. [PubMed: 10390518]
2. DiPolo R, Beauge L. Sodium/calcium exchanger: influence of metabolic regulation on ion carrier interactions. Physiol Rev. 2006; 86:155–203. [PubMed: 16371597]
3. Clapham DE. Calcium signaling. Cell. 2007; 131:1047–1058. [PubMed: 18083096]
4. Berridge MJ, Bootman MD, Roderick HL. Calcium signalling: dynamics, homeostasis and remodelling. Nat Rev Mol Cell Biol. 2003; 4:517–529. [PubMed: 12838335]
5. Hilgemann DW. Unitary cardiac $Na^+$, $Ca^{2+}$ exchange current magnitudes determined from channel-like noise and charge movements of ion transport. Biophys J. 1996; 71:759–768. [PubMed: 8842214]
6. Hilgemann DW, Nicoll DA, Philipson KD. Charge movement during $Na^+$ translocation by native and cloned cardiac $Na^+/Ca^{2+}$ exchanger. Nature. 1991; 352:715–718. [PubMed: 1876186]
7. Reeves JP, Hale CC. The stoichiometry of the cardiac sodium-calcium exchange system. J Biol Chem. 1984; 259:7733–7739. [PubMed: 6736024]
8. Blaustein MP, Russell JM. Sodium-calcium exchange and calcium-calcium exchange in internally dialyzed squid giant axons. J Membr Biol. 1975; 22:285–312. [PubMed: 1159780]
9. Rasgado-Flores H, Blaustein MP. Na/Ca exchange in barnacle muscle cells has a stoichiometry of 3 $Na^+$/1 $Ca^{2+}$. Am J Physiol. 1987; 252:C499–504. [PubMed: 3578502]
10. Kimura J, Noma A, Irisawa H. Na-Ca exchange current in mammalian heart cells. Nature. 1986; 319:596–597. [PubMed: 3945347]
11. Kang TM, Hilgemann DW. Multiple transport modes of the cardiac $Na^+/Ca^{2+}$ exchanger. Nature. 2004; 427:544–548. [PubMed: 14765196]
12. Jardetzky O. Simple allosteric model for membrane pumps. Nature. 1966; 211:969–970. [PubMed: 5968307]
13. Hilgemann DW. Regulation and deregulation of cardiac $Na^+$-$Ca^{2+}$ exchange in giant excised sarcolemmal membrane patches. Nature. 1990; 344:242–245. [PubMed: 2314460]
14. Matsuoka S, Nicoll DA, Reilly RF, Hilgemann DW, Philipson KD. Initial localization of regulatory regions of the cardiac sarcolemmal $Na^+$-$Ca^{2+}$ exchanger. Proc Natl Acad Sci USA. 1993; 90:3870–3874. [PubMed: 8483905]
15. Philipson KD, Nicoll DA. Sodium-calcium exchange: a molecular perspective. Annu Rev Physiol. 2000; 62:111–133. [PubMed: 10845086]
16. Nicoll DA, Hryshko LV, Matsuoka S, Frank JS, Philipson KD. Mutation of amino acid residues in the putative transmembrane segments of the cardiac sarcolemmal $Na^+$-$Ca^{2+}$ exchanger. J Biol Chem. 1996; 271:13385–13391. [PubMed: 8662775]
17. Nicoll DA, Ottolia M, Philipson KD. Toward a topological model of the NCX1 exchanger. Ann N Y Acad Sci. 2002; 976:11–18. [PubMed: 12502529]
18. Ren X, Nicoll DA, Xu L, Qu Z, Philipson KD. Transmembrane segment packing of the $Na^+/Ca^{2+}$ exchanger investigated with chemical cross-linkers. Biochemistry. 2010; 49:8585–8591. [PubMed: 20735122]
19. Cai X, Lytton J. The cation/$Ca^{2+}$ exchanger superfamily: phylogenetic analysis and structural implications. Mol Biol Evol. 2004; 21:1692–1703. [PubMed: 15163769]
20. Liao J, et al. Structural insight into the ion-exchange mechanism of the sodium/calcium exchanger. Science. 2012; 335:686–690. [PubMed: 22323814]
21. Almagor L, et al. Functional asymmetry of bidirectional $Ca^{2+}$-movements in an archaeal sodium-calcium exchanger (NCX_Mj). Cell Calcium. 2014; 56:276–284. [PubMed: 25218934]
22. Marinelli F, et al. Sodium recognition by the $Na^+/Ca^{2+}$ exchanger in the outward-facing conformation. Proc Natl Acad Sci USA. 2014; 111:E5354–5362. [PubMed: 25468964]

23. Blaustein MP, Santiago EM. Effects of internal and external cations and of ATP on sodium-calcium and calcium-calcium exchange in squid axons. Biophys J. 1977; 20:79–111. [PubMed: 901903]
24. Trosper TL, Philipson KD. Effects of divalent and trivalent cations on $Na^+$-$Ca^{2+}$ exchange in cardiac sarcolemmal vesicles. Biochim Biophys Acta. 1983; 731:63–68. [PubMed: 6849912]
25. DiPolo R, Beauge L. Asymmetrical properties of the Na-Ca exchanger in voltage-clamped, internally dialyzed squid axons under symmetrical ionic conditions. J Gen Physiol. 1990; 95:819–835. [PubMed: 2362183]
26. Matsuoka S, Hilgemann DW. Steady-state and dynamic properties of cardiac sodium-calcium exchange. Ion and voltage dependencies of the transport cycle. J Gen Physiol. 1992; 100:963–1001. [PubMed: 1336540]
27. Miura Y, Kimura J. Sodium-calcium exchange current. Dependence on internal $Ca^{2+}$ and $Na^+$ and competitive binding of external $Na^+$ and $Ca^{2+}$. J Gen Physiol. 1989; 93:1129–1145. [PubMed: 2549177]
28. Waight AB, et al. Structural basis for alternating access of a eukaryotic calcium/proton exchanger. Nature. 2013; 499:107–110. [PubMed: 23685453]
29. Nishizawa T, et al. Structural basis for the counter-transport mechanism of a $H^+$/$Ca^{2+}$ exchanger. Science. 2013; 341:168–172. [PubMed: 23704374]
30. Wu M, et al. Crystal structure of $Ca^{2+}$/$H^+$ antiporter protein YfkE reveals the mechanisms of $Ca^{2+}$ efflux and its pH regulation. Proc Natl Acad Sci USA. 2013; 110:11367–11372. [PubMed: 23798403]
31. Giladi M, et al. Asymmetric preorganization of inverted pair residues in the sodium-calcium exchanger. Sci. Rep. 2016; 6:20753. [PubMed: 26876271]
32. Iwamoto T, Uehara A, Imanaga I, Shigekawa M. The $Na^+$/$Ca^{2+}$ exchanger NCX1 has oppositely oriented reentrant loop domains that contain conserved aspartic acids whose mutation alters its apparent $Ca^{2+}$ affinity. J. Biol. Chem. 2000; 275:38571–38580. [PubMed: 10967097]
33. John SA, Liao J, Jiang Y, Ottolia M. The cardiac $Na^+$-$Ca^{2+}$ exchanger has two cytoplasmic ion permeation pathways. Proc. Natl. Acad. Sci. USA. 2013; 110:7500–7505. [PubMed: 23589872]
34. Ottolia M, Nicoll DA, Philipson KD. Mutational analysis of the alpha-1 repeat of the cardiac $Na^+$-$Ca^{2+}$ exchanger. J. Biol. Chem. 2005; 280:1061–1069. [PubMed: 15519995]
35. Reeves JP, Sutko JL. Competitive interactions of sodium and calcium with the sodium-calcium exchange system of cardiac sarcolemmal vesicles. J Biol Chem. 1983; 258:3178–3182. [PubMed: 6826556]
36. Caffrey M, Cherezov V. Crystallizing membrane proteins using lipidic mesophases. Nat Protoc. 2009; 4:706–31. [PubMed: 19390528]
37. Otwinowski Z, Minor W. Processing of X-ray diffraction data collected in oscillation mode. Methods Enzymol. 1997; 276:307–326.
38. McCoy AJ, et al. Phaser crystallographic software. J Appl Crystallogr. 2007; 40:658–674. [PubMed: 19461840]
39. Emsley P, Cowtan K. Coot: model-building tools for molecular graphics. Acta Crystallogr D Biol Crystallogr. 2004; 60:2126–32. [PubMed: 15572765]
40. Adams PD, et al. PHENIX: a comprehensive Python-based system for macromolecular structure solution. Acta Crystallogr D Biol Crystallogr. 2010; 66:213–21. [PubMed: 20124702]
41. Petrek M, et al. CAVER: a new tool to explore routes from protein clefts, pockets and cavities. BMC Bioinformatics. 2006; 7:316. [PubMed: 16792811]
42. Phillips JC, et al. Scalable molecular dynamics with NAMD. J. Comp. Chem. 2005; 26:1781–1802. [PubMed: 16222654]
43. MacKerell AD, et al. All-atom empirical potential for molecular modeling and dynamics studies of proteins. J. Phys. Chem. B. 1998; 102:3586–3616. [PubMed: 24889800]
44. Mackerell AD, Feig M, Brooks CL. Extending the treatment of backbone energetics in protein force fields: Limitations of gas-phase quantum mechanics in reproducing protein conformational distributions in molecular dynamics simulations. J. Comp. Chem. 2004; 25:1400–1415. [PubMed: 15185334]

45. Staritzbichler R, Anselmi C, Forrest LR, Faraldo-Gomez JD. GRIFFIN: A versatile methodology for optimization of protein-lipid interfaces for membrane protein simulations. J. Chem. Theor. Comp. 2011; 7:1167–1176.
46. Piana S, Laio A. A bias-exchange approach to protein folding. J. Phys. Chem. B. 2007; 111:4553–9. [PubMed: 17419610]
47. Branduardi D, Bussi G, Parrinello M. Metadynamics with adaptive gaussians. J. Chem. Theor. Comp. 2012; 8:2247–2254.
48. Hess B, Kutzner C, van der Spoel D, Lindahl E. GROMACS 4: Algorithms for highly efficient, load-balanced, and scalable molecular simulation. J. Chem. Theor. Comp. 2008; 4:435–447.
49. Bonomi M, et al. PLUMED: A portable plugin for free-energy calculations with molecular dynamics. Comp. Phys. Commun. 2009; 180:1961–1972.
50. Branduardi D, Gervasio FL, Parrinello M. From A to B in free energy space. J. Chem. Phys. 2007; 126:054103. [PubMed: 17302470]
51. Kumar S, Bouzida D, Swendsen RH, Kollman PA, Rosenberg JM. The Weighted Histogram Analysis Method for free-energy calculations on biomolecules .1. The method. J. Comp. Chem. 1992; 13:1011–1021.
52. Biarnes X, Pietrucci F, Marinelli F, Laio A. METAGUI: A VMD interface for analyzing metadynamics and molecular dynamics simulations. Comp. Phys. Commun. 2012; 183:203–211.
53. Corbi-Verge C, et al. Two-state dynamics of the SH3-SH2 tandem of Abl kinase and the allosteric role of the N-cap. Proc. Natl. Acad. Sci. USA. 2013; 110:E3372–E3380. [PubMed: 23959873]
54. Daura X, et al. Peptide folding: When simulation meets experiment. Angew. Chem. Int. Edit. 1999; 38:236–240.
55. Branduardi D, Marinelli F. Faraldo-Gómez, J.D. Atomic-resolution dissection of the energetics and mechanism of isomerization of hydrated ATP-Mg through the SOMA string method. J. Comput. Chem. 2015 in press.
56. Enright AJ, Van Dongen S, Ouzounis CA. An efficient algorithm for large-scale detection of protein families. Nucleic Acids Res. 2002; 30:1575–1584. [PubMed: 11917018]

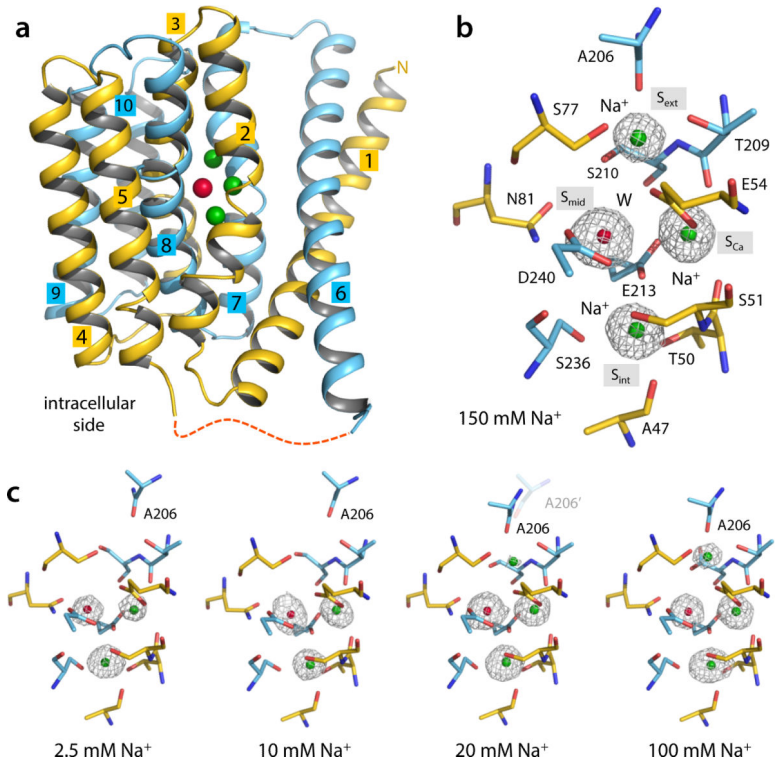


**Figure 1.**

$Na^+$ binding to outward-facing NCX_Mj. (**a**) Overall structure of native outward-facing NCX_Mj from crystals grown in 150 mM $Na^+$. N- and C-terminal halves are colored yellow and cyan, respectively. Colored spheres represent the bound $Na^+$ (green) and water (red). (**b**) Structural details and definition of the four central binding sites. Only residues flanking these sites are shown for clarity (same for all other figures). The electron density (grey mesh, 1.9 Å $F_o$-$F_c$ ion omit map contoured at 4σ) at $S_{mid}$ was modeled as water (red sphere) and those at $S_{ext}$, $S_{Ca}$ and $S_{int}$ as $Na^+$ ions (green spheres). Further details are shown in **Supplementary Fig. 1**. (**c**) Concentration-dependent change in $Na^+$ occupancy (see also **Table 1**). All $F_o$ – $F_c$ ion-omit maps are calculated to 2.4 Å and contoured at 3σ for comparison. The displacement of A206 reflects the [$Na^+$]-dependent conformational change from the partially open to the occluded state (observed at low and high $Na^+$ concentrations, respectively). At 20 mM $Na^+$, both conformations co-exist. No significant changes were observed in the side-chains involved in ion or water coordination at the $S_{Ca}$, $S_{int}$ and $S_{mid}$ sites.

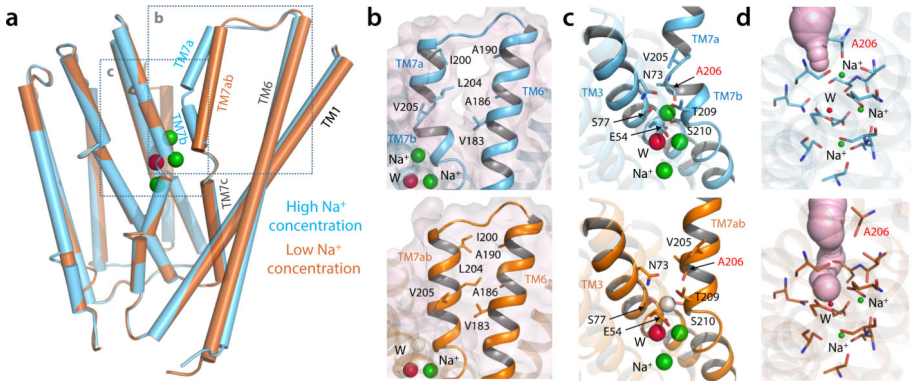


**Figure 2.**

$Na^+$-occupancy dependent conformational change in NCX_Mj. (**a**) Superimposition of the NCX_Mj crystal structures obtained in high (100 mM, cyan cylinders) and low (10 mM, brown cylinders) $Na^+$ concentrations. (**b**) Close-up view of the interface between TM6 and TM7ab in the NCX_Mj structures obtained at high and low $Na^+$ concentrations (top and lower panels, respectively). Residues forming van-der-Waals contacts in the structure at low $Na^+$ concentration are shown in detail. (**c**) Close-up view of the $Na^+$-binding sites. The vacant $S_{ext}$ site in the structure at low $Na^+$ concentration is indicated with a white sphere. Residues surrounding this site are also indicated; note A206 (labeled in red) coordinates $Na^+$ at $S_{ext}$ via its backbone carbonyl oxygen. (**d**) Extracellular solvent accessibility of the ion binding sites in the structures at high and low [$Na^+$]. Putative solvent channels are represented as light-purple surfaces.

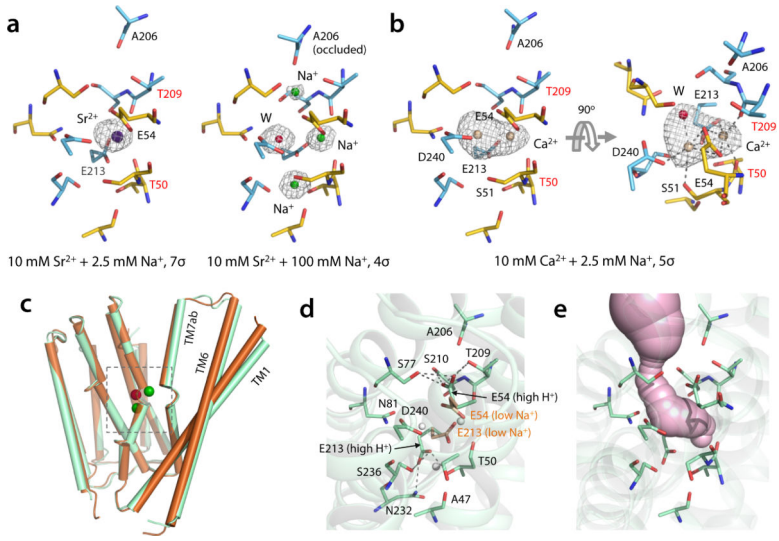


**Figure 3.**

Divalent cation binding and apo structure of NCX_Mj. (**a**) A single $Sr^{2+}$ (dark blue sphere) binds at $S_{Ca}$ in crystals titrated with 10 mM $Sr^{2+}$ and 2.5 mM $Na^{+}$ (see also **Supplementary Fig. 2**). Residues involved in $Sr^{2+}$ coordination are labeled. There are no significant changes in the side-chains involved in ion coordination, relative to the $Na^{+}$-bound state. T50 and T209 (labeled in red) coordinate $Sr^{2+}$ through their backbone carbonyl-oxygen atoms. High $Na^{+}$ concentration (100 mM) completely displaces $Sr^{2+}$ and reverts NCX_Mj to the occluded state (right panel). The contour level of the $F_o - F_c$ omit map of the structure at high $Na^{+}$ concentration was lowered (to 4σ) so as to visualize the density from $Na^{+}$ ions and $H_2O$. (**b**) $Ca^{2+}$ (tanned spheres) binds either to $S_{Ca}$ or $S_{mid}$ in crystals titrated with 10 mM $Ca^{2+}$ and 2.5 mM $Na^{+}$ (see also **Supplementary Fig. 2**). The relative occupancies are 55% and 45%, respectively. (**c**) Superimposition of NCX_Mj structures obtained at low $Na^{+}$ concentration (10 mM) and pH 6.5 (brown) and in the absence of $Na^{+}$ and pH 4 (light green), referred to as apo state. (**d**) Close-up view of the ion-binding sites in the apo (or high $H^{+}$) state. The side chains of E54 and E213 from the low $Na^{+}$ structure are also shown (light brown) for comparison. White spheres indicate the location $S_{int}$, $S_{mid}$ $S_{Ca}$. (**e**) Extracellular solvent accessibility of the ion-binding sites in apo NCX_Mj.

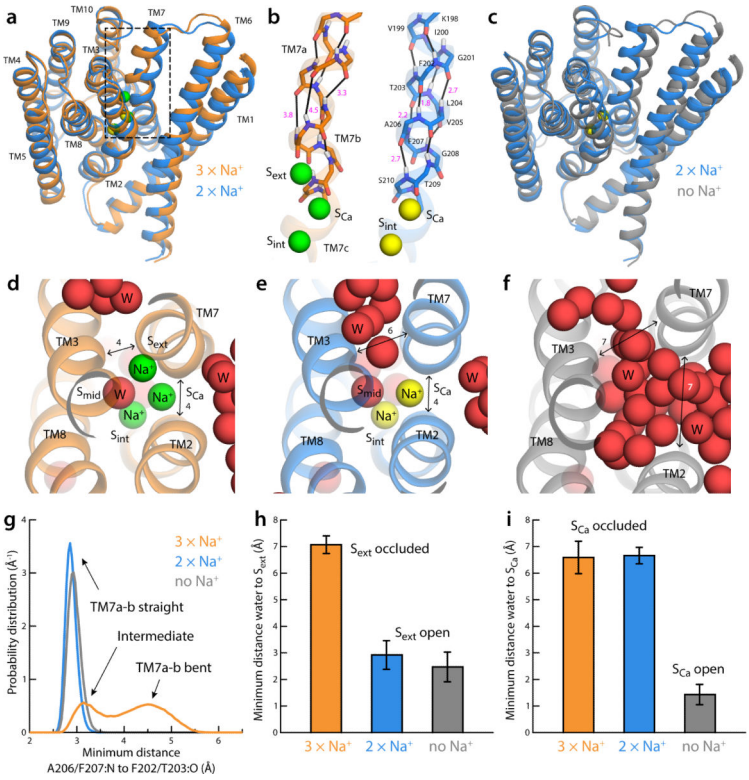


**Figure 4.**

Spontaneous changes in the structure of outward-occluded, fully $Na^+$-occupied NCX_Mj (PDB code 3V5U[20]) upon sequential displacement of $Na^+$. (**a**) Representative simulation snapshots of NCX_Mj (**Methods**) with $Na^+$ bound at $S_{ext}$, $S_{Ca}$ and $S_{int}$ (orange cartoons, green spheres) and with $Na^+$ bound only at $S_{Ca}$ and $S_{int}$ (marine cartoons, yellow spheres) (**b**) Close-up of the backbone of the N-terminal half of TM7 (TM7ab), in the same $Na^+$ occupancy states depicted in (a). Black lines indicate (*i*, *i* + 4) carbonyl-amide pairs along the helix; specific O-N distances are indicated, in Å (magenta). (**c**) Representative simulation snapshots (same as above) with $Na^+$ bound at $S_{Ca}$ and $S_{int}$ (marine cartoons, yellow spheres) and without any $Na^+$ bound (grey cartoons). (**d**) Close-up of the ion-binding region in the fully $Na^+$-occupied state. Approximate distances between TM2, TM3 and TM7 are indicated in Å. (**e**) Close-up of the ion-binding region in the partially $Na^+$-occupied state. (**f**) Close-up of the ion-binding region in the $Na^+$-free state. (**g-i**) Analytical descriptors of the changes just described, calculated from the simulations of each $Na^+$-occupancy state depicted in panels (a-f). These descriptors were employed as collective variables in the Bias-Exchange Metadynamics simulations (**Methods**). (**g**) Probability distributions of an analytical descriptor of the backbone hydrogen-bonding pattern in TM7ab (**Eq. 2**). (**h**) Mean value (with standard deviation) of a quantitative descriptor of the solvent accessibility of the $S_{ext}$ site (**Eq. 1**). (**i**) Mean value (with standard deviation) of a quantitative descriptor of the solvent accessibility of the $S_{Ca}$ site (**Eq. 1**).

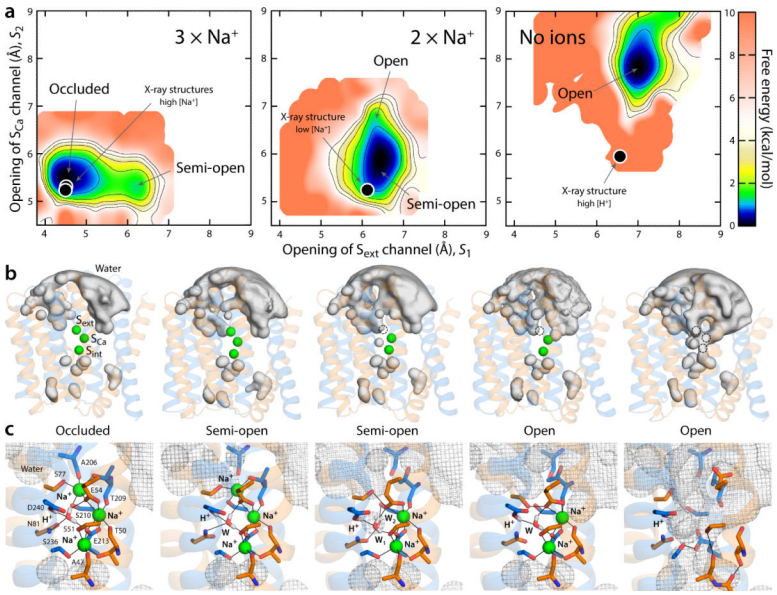


**Figure 5.**

Thermodynamic basis for the proposed mechanism of substrate control of the alternating-access transition of NCX. (**a)** Calculated conformational free-energy landscapes for outward-facing NCX_Mj, for two different $Na^+$-occupancy states, and for a state with no ions bound. The free energy is plotted as a function of two coordinates, each describing the degree of opening of the aqueous channels leading to the $S_{ext}$ and $S_{Ca}$ sites, respectively (see Methods). Contours correspond to 1 kcal/mol intervals. Black circles map the X-ray structures of NCX_Mj obtained at high and low $Na^+$ concentration, as well as that at low pH, reported in this study. (**b**) Density isosurfaces for water molecules within 12 Å of the ion-binding region (grey volumes), for each of the major conformational free-energy minima in each ion-occupancy state. $Na^+$ ions are shown as green spheres. The two inverted-topology repeats in the transporter structure (transparent cartoons) are colored differently (TM1-5, orange; TM6-10, marine). (**c**) Close-up views of the ion-binding region in the same conformational free-energy minima. Key residues involved in $Na^+$ and water coordination (W) are highlighted (sticks, black lines). The water-density maps in (b) is shown here as a grey mesh. Note D240 is protonated, while E54 and E213 are ionized[22].

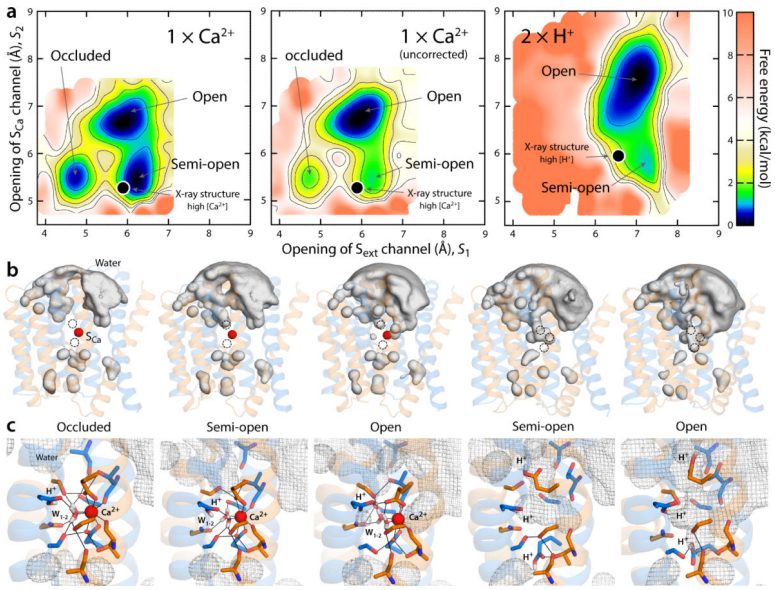


**Figure 6.**

Thermodynamic basis for the proposed mechanism of substrate control of the alternating-access transition of NCX. (**a**) Calculated free-energy landscapes for outward-facing NCX_Mj, for the $Ca^{2+}$ and the fully protonated state. The free energy is plotted as in **Fig. 5**. For $Ca^{2+}$, a map is shown in which a correction for the charge-transfer between the ion and the protein is introduced, alongside the uncorrected map (see **Supplementary Notes 3-4** and **Supplementary Fig. 5-6**). The uncorrected map overstabilizes the open state relative to the semi-open and occluded because it also overestimates the cost of dehydration of the ion, once it is bound to the protein (this effect is negligible for $Na^{+}$). Black circles map the crystal structures obtained at high $Ca^{2+}$ concentration and at low pH (or high $H^{+}$) reported in this study. (**b**) Water-density isosurfaces analogous to those in **Fig. 5** are shown for each of the major conformational free-energy minima in the free-energy maps. The $Ca^{2+}$ ion is shown as a red sphere; the protein is shown as in **Fig. 5**. (**c**) Close-up views of the ion-binding region in the same conformational free-energy minima. Key residues involved in $Ca^{2+}$ and water coordination (W) are highlighted (sticks, black lines). The water-density maps in (b) are shown here as a grey mesh. In the occluded state with $Ca^{2+}$ bound, helix TM7ab bends in the same way as in the fully occupied $Na^{+}$ state, as the carbonyl of Ala206 forms a hydrogen-bonding interaction with Ser210.

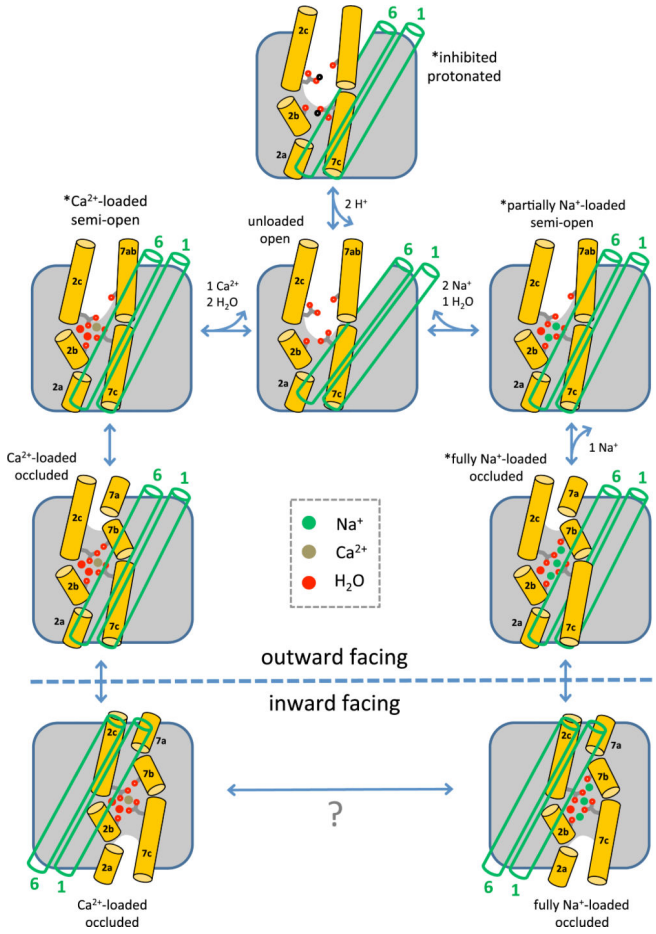


**Figure 7.**

Structural mechanism of extracellular forward ion exchange in NCX. The carbonyl groups of Ala47 (on TM2b) and Ala206 (on TM7b), and the side chains of Glu54 (on TM2c) and Glu213 (on TM7c) are highlighted; these are four of the key residues for ion chelation and conformational changes. The green open cylinders represent the gating helices TM1 and TM6. Asterisks mark the states whose crystal structures have been determined in this study. These states and their connectivity can also be deduced from the calculated free-energy landscapes, which also reveal a $Ca^{2+}$-loaded outward-facing occluded state, and an unloaded, fully open state.

## Table 1

Concentration-dependent $Na^+$ occupancy of outward-facing NCX_Mj

| **Sites \ [$Na^+$]** | **2.5 mM** | **10 mM** | **20 mM** | **100 mM** | **150 mM** |
|---|---|---|---|---|---|
| $S_{int}$ | 0.84 | 0.92 | 0.99 | 0.96 | 1.00 |
| $S_{Ca}$ | 0.75 | 0.87 | 0.97 | 1.00 | 1.00 |
| $S_{ext}$ | - | - | 0.59 | 0.79 | 0.93 |
| Total | 1.58 | 1.79 | 2.55 | 2.75 | 2.93 |
| Conformation | Partially open | Partially open | Mixed | Occluded | Occluded |

## Table 2

Data collection and refinement statistics for the NCX_Mj structures obtained from crystals soaked with varying amounts of $Na^+$, and no $Ca^{2+}$, and at low pH and no $Na^+$ or $Ca^{2+}$.

| [$Na^+$] | 2.5 mM PDB 5HWX | 10 mM PDB 5HWY | 20 mM PDB 5HXC | 100 mM PDB 5HXE | 150 mM PDB 5HYA | 0 mM PDB 5HXH |
|---|---|---|---|---|---|---|
| **Data collection** | | | | | | |
| Space group | P212121 | | | | | C2 |
| Cell dimensions | | | | | | |
| a, b, c (Å) | 49.70, 72.28, 95.78 | 46.21, 71.97, 95.63 | 49.75, 72.56, 95.78 | 49.77, 72.85, 96.36 | 49.49, 72.88, 96.21 | 164.18, 46.83, 96.96 |
| α, β, γ (°) | 90, 90, 90 | 90, 90, 90 | 90, 90, 90 | 90, 90, 90 | 90, 90, 90 | 90, 106.20, 90 |
| Resolution (Å) | 2.40 (2.44-2.40) | 2.10 (2.14-2.10) | 2.10 (2.14-2.10) | 2.28 (2.32-2.28) | 1.90 (1.93-1.90) | 2.80 (2.85-2.80) |
| $R_{sym}$ (%) | 9.4 (99.4) | 9.3 (69.8) | 10.5 (99.6) | 9.9 (56.3) | 8.6 (88.0) | 10.5 (94.3) |
| I/σI | 24.2 (1.8) | 24.3 (2.7) | 20.6 (1.9) | 15.9 (2.8) | 32.9 (2.4) | 17.7 (1.2) |
| $CC_{1/2}$ | (0.625) | (0.819) | (0.602) | (0.722) | (0.786) | (0.561) |
| Completeness (%) | 99.8 (99.1) | 99.9 (100) | 99.9 (99.8) | 96.4 (98.6) | 98.9 (97.8) | 99.9 (99.9) |
| Redundancy | 6.9 (6.7) | 6.1 (6.0) | 7.1 (7.0) | 3.4 (3.3) | 9.3 (8.9) | 7.1 (5.7) |
| **Refinement** | | | | | | |
| Resolution (Å) | 50-2.4 | 50-2.1 | 50-2.1 | 50-2.3 | 50-1.9 | 50-2.80 |
| No. reflections | 13977 | 19254 | 20739 | 15767 | 27923 | 21489 |
| $R_{work}/R_{free}$ | 0.21/0.25 | 0.19/0.22 | 0.19/0.23 | 0.19/0.24 | 0.179/0.207 | 0.20/0.26 |
| **No. atoms** | | | | | | |
| Protein | 2206 | 2274 | 2366 | 2229 | 2229 | 4410 |
| Ligand/Ion | 56/3 | 154/2 | 161/5 | 162/6 | 257/4 | 121/2 |
| Water | 18 | 36 | 67 | 67 | 100 | 39 |
| **B-factors** | | | | | | |
| Protein | 53.25 | 34.28 | 34.91 | 39.75 | 26.05 | 42.98 |
| Ligand/Ion | 62.94/47.70 | 55.86/31.75 | 55.25/36.47 | 58.24/38.93 | 46.11/22.13 | 54.29/63.47 |
| Water | 58.12 | 41.16 | 46.97 | 49.74 | 37.80 | 33.17 |
| **R.m.s deviations** | | | | | | |
| Bond lengths (Å) | 0.004 | 0.006 | 0.008 | 0.003 | 0.006 | 0.003 |
| Bond angles (°) | 0.819 | 0.915 | 1.269 | 1.024 | 0.966 | 0.705 |

Values in parenthesis are for highest resolution shell. 5% of the data was used in the $R_{free}$ calculation. 'Ligand' atoms are from lipids, PEG400 and acetates.

## Table 3

Data collection and refinement statistics for the NCX_Mj structures obtained from crystals soaked with varying amounts of $Na^+$ and $Sr^{2+}$.

| **[$Sr^{2+}$] / [$Na^+$]** | **10 mM / 2.5 mM PDB 5HXS** | **1 mM / 2.5 mM N/A*** | **0.1 mM / 2.5 mM N/A*** | **10 mM / 10 mM N/A*** | **10 mM / 100 mM N/A#** |
|---|---|---|---|---|---|
| **Data collection** | | | | | |
| Space group | P212121 | | | | |
| Cell dimensions | | | | | |
| a, b, c (Å) | 49.52, 72.35, 96.00 | 49.76, 72.62, 95.62 | 49.80, 72.27, 94.84 | 49.67, 72.46, 96.43 | 49.88, 72.43, 95.91 |
| α, β, γ (°) | 90, 90, 90 | 90, 90, 90 | 90, 90, 90 | 90, 90, 90 | 90, 90, 90 |
| Resolution (Å) | 2.80 (2.85-2.80) | 2.90 (2.95-2.90) | 2.54 (2.58-2.54) | 2.30 (2.34-2.30) | 2.50 (2.54-2.50) |
| $R_{sym}$ (%) | 12.3 (88.0) | 12.3 (91.0) | 11.9 (88.5) | 13.7 (95.8) | 10.9 (96.8) |
| I/σI | 19.0 (1.8) | 19.2 (1.6) | 21.5 (1.9) | 18.4 (1.6) | 19.7 (1.8) |
| $CC_{1/2}$ | (0.674) | (0.686) | (0.768) | (0.420) | (0.767) |
| Completeness (%) | 98.8 (90.4) | 94.9 (96.1) | 99.9 (100.0) | 99.8 (99.9) | 99.6 (99.7) |
| Redundancy | 6.5 (5.4) | 6.7 (6.9) | 7.1 (6.8) | 6.2 (4.5) | 5.9 (6.0) |
| **Refinement** | | | | | |
| Resolution (Å) | 50-2.80 | 50-2.90 | 50-2.54 | 50-2.3 | 50-2.5 |
| No. reflections | 8927 | 7611 | 11483 | 16488 | 12665 |
| $R_{work}/R_{free}$ | 0.22/0.27 | 0.22/0.27 | 0.23/0.26 | 0.20/0.25 | 0.21/0.24 |
| **No. atoms** | | | | | |
| Protein | 2227 | 2249 | 2217 | 2271 | 2223 |
| Ligand/Ion | 110/2 | 133/3 | 155/3 | 101/3 | 104/6 |
| Water | 10 | 2 | 5 | 34 | 17 |
| **B-factors** | | | | | |
| Protein | 61.55 | 67.82 | 60.83 | 46.42 | 56.75 |
| Ligand/Ion | 74.56/63.32 | 85.56/70.47 | 80.33/90.41 | 64.79/38.25 | 71.27/53.50 |
| Water | 59.22 | 61.31 | 68.58 | 51.39 | 55.07 |
| **R.m.s deviations** | | | | | |
| Bond lengths (Å) | 0.004 | 0.005 | 0.005 | 0.007 | 0.003 |
| Bond angles (°) | 0.887 | 1.076 | 0.963 | 1.057 | 0.733 |

Values in parenthesis are for highest resolution shell. 5% of the data was used in the $R_{free}$ calculation. 'Ligand' atoms are from lipids, PEG400 and acetates.

*These structures are virtually identical to that resolved with 10 mM $Sr^{2+}$ (PDB 5HXS), except for the weakened electron-density signal for the divalent ion, and were therefore not deposited in the PDB.

#This structure is virtually identical to that resolved with 100 mM $Na^+$ without $Ca^{2+}$ or $Sr^{2+}$ (Table 1, PDB 5HXE) and was therefore not deposited in the PDB.

## Table 4

Data collection and refinement statistics for the NCX_Mj structures obtained from crystals soaked with varying amounts of $Na^+$ and $Ca^{2+}$.

| **[$Ca^{2+}$] / [$Na^+$]** | **10 mM / 2.5 mM PDB 5HXR** | **1 mM / 2.5 mM N/A*** | **0.1 mM / 2.5 mM N/A*** | **10 mM / 10 mM N/A*** |
|---|---|---|---|---|
| **Data collection** | | | | |
| Space group | P212121 | | | |
| Cell dimensions | | | | |
| a, b, c (Å) | 49.70, 72.52, 96.94 | 49.80, 72.26, 95.80 | 49.48, 72.47, 96.30 | 49.88, 72.22, 96.10 |
| α, β, γ (°) | 90, 90, 90 | 90, 90, 90 | 90, 90, 90 | 90, 90, 90 |
| Resolution (Å) | 2.45 (2.49-2.45) | 2.65 (2.70-2.65) | 2.40 (2.44-2.40) | 2.20 (2.24-2.20) |
| $R_{sym}$ (%) | 11.8 (94.2) | 11.1 (92.1) | 11.2 (91.3) | 10.3 (99.1) |
| I/σI | 24.4 (1.6) | 20.9 (1.6) | 20.4 (1.6) | 22.4 (1.8) |
| $CC_{1/2}$ | (0.611) | (0.696) | (0.632) | (0.549) |
| Completeness (%) | 99.7 (100.0) | 99.9 (100.0) | 99.2 (100.0) | 99.7 (100.0) |
| Redundancy | 7.8 (7.8) | 7.0 (6.5) | 6.9 (7.0) | 7.1 (7.1) |
| **Refinement** | | | | |
| Resolution (Å) | 50-2.45 | 50-2.65 | 50-2.40 | 50-2.2 |
| No. reflections | 12996 | 10548 | 13736 | 18080 |
| $R_{work}/R_{free}$ | 0.22/0.26 | 0.22/0.28 | 0.20/0.26 | 0.19/0.24 |
| **No. atoms** | | | | |
| Protein | 2211 | 2225 | 2228 | 2284 |
| Ligand/Ion | 114/3 | 130/3 | 162/3 | 164/4 |
| Water | 16 | 20 | 42 | 57 |
| **B-factors** | | | | |
| Protein | 64.97 | 71.22 | 53.50 | 45.16 |
| Ligand/Ion | 78.98/60.53 | 90.03/72.90 | 70.67/45.53 | 69.09/42.92 |
| Water | 68.57 | 81.02 | 64.12 | 55.45 |
| **R.m.s deviations** | | | | |
| Bond lengths (Å) | 0.002 | 0.004 | 0.002 | 0.004 |
| Bond angles (°) | 0.630 | 1.143 | 0.686 | 0.650 |

Values in parenthesis are for highest resolution shell. 5% of the data was used in the $R_{free}$ calculation. 'Ligand' atoms are from lipids, PEG400 and acetates.

*These structures are virtually identical to that resolved with 10 mM $Ca^{2+}$ and 2.5 mM $Na^+$ (PDB 5HXR), except for the weakened electron-density signal for the divalent ion, and were therefore not deposited in the PDB.